

A Plug-and-Play Method for Guided Multi-contrast MRI Reconstruction based on Content/Style Modeling

Chinmay Rao^{a,*}, Matthias van Osch^a, Nicola Pezzotti^{b,c}, Jeroen de Bresser^a, Laurens Beljaards^a, Jakob Meineke^d, Elwin de Weerd^e, Huangling Lu^a, Mariya Doneva^d, Marius Staring^a

^a*Department of Radiology, Leiden University Medical Center, Leiden, The Netherlands*

^b*Cardiologs, Paris, France*

^c*Department of Mathematics and Computer Science, Eindhoven University of Technology, Eindhoven, The Netherlands*

^d*Philips Innovative Technologies, Hamburg, Germany*

^e*Philips, Best, The Netherlands*

Abstract

Since multiple MRI contrasts of the same anatomy contain redundant information, one contrast can guide the reconstruction of an undersampled subsequent contrast. To this end, several end-to-end learning-based guided reconstruction methods have been proposed. However, a key challenge is the requirement of large paired training datasets comprising raw data and aligned reference images. We propose a modular two-stage approach addressing this issue, additionally providing an explanatory framework for the multi-contrast problem based on the shared and non-shared generative factors underlying two given contrasts. A content/style model of two-contrast image data is learned from a largely unpaired image-domain dataset and is subsequently applied as a plug-and-play operator in iterative reconstruction. The disentanglement of content and style allows explicit representation of contrast-independent and contrast-specific factors. Consequently, incorporating prior information into the reconstruction reduces to a simple replacement of the aliased content of the reconstruction iterate with high-quality content derived from the reference scan. Combining this component with a data consistency step and introducing a general corrective process for the content yields an iterative scheme. We name this novel approach PnP-CoSMo. Various aspects like interpretability and convergence are explored via simulations. Furthermore, its practicality is demonstrated on the NYU fastMRI DICOM dataset, showing improved generalizability compared to end-to-end methods, and on two in-house multi-coil raw datasets, offering up to 32.6% more acceleration over learning-based non-guided reconstruction for a given SSIM. In a small radiological task, PnP-CoSMo allowed 33.3% more acceleration over clinical reconstruction at diagnostic quality.

Keywords: MRI reconstruction, multi-modal, content/style decomposition, plug-and-play

1. Introduction

Magnetic resonance imaging (MRI) is an invaluable medical imaging modality due to the high-quality scans it delivers, the variety of complementary information it can capture, and its lack of radiation-related risks, leading to its wide usage in clinical practice. However, its central limitation is the inherently slow data acquisition process. The raw sensor data is acquired in the frequency domain, or k-space, from which the image is reconstructed. Over the last 25 years, advancements such as parallel imaging (Pruessmann et al., 2001; Griswold et al., 2002), compressed sensing (CS) (Lustig et al., 2007), and deep learning reconstruction (Aggarwal et al., 2018; Pezzotti et al., 2020) have enabled considerable speedups by allowing sub-Nyquist

*c.s.rao@lumc.nl

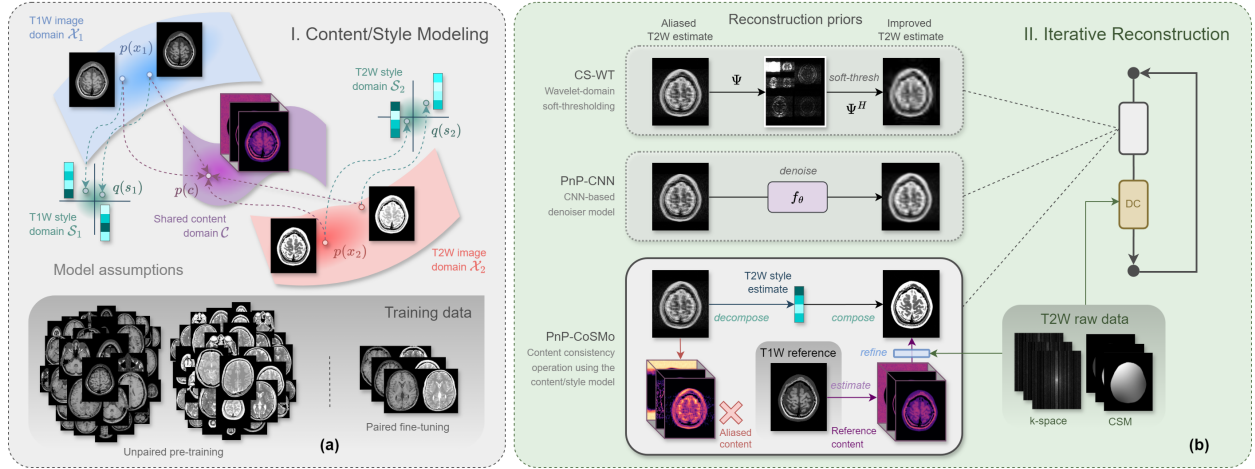


Figure 1: Our two-stage approach to guided reconstruction. (a) The first stage learns a content/style model of two-contrast MR image data. We assume that the two image domains \mathcal{X}_1 and \mathcal{X}_2 can be decomposed into a shared content domain \mathcal{C} and separate style domains \mathcal{S}_1 and \mathcal{S}_2 . This model is learned in two stages – an unpaired pre-training stage and a paired fine-tuning stage, both requiring only image data. (b) The reconstruction stage applies the content/style model as a *content consistency operator* (bottom) within an ISTA-based iterative scheme. Given an aligned reference image, guidance is introduced into the reconstruction by simply replacing its aliased content with content derived from the reference. The "refine" block denotes a content refinement update, which iteratively corrects for inconsistencies between the reference content and the measured k-space data, improving the effectiveness of the content consistency operator. DC denotes data consistency. For comparison, two other reconstruction priors are shown, namely wavelet-domain soft-thresholding (top) and CNN-based denoising (middle) used in CS and PnP-CNN algorithms, respectively.

k-space sampling and relying on computationally sophisticated reconstruction. These techniques have subsequently been implemented on commercial MRI systems and have demonstrated (potential) improvements in clinical workflow (Seow et al., 2024).

A clinical MRI session typically involves the acquisition of multiple scans of the same anatomy through the application of different MR pulse sequences, exhibiting different contrasts. Because these scans are different reflections of the same underlying reality, they share a high degree of shared structure. However, currently deployed clinical protocols acquire and reconstruct each scan as an independent measurement, not leveraging the information redundancy across scans. There is, therefore, an opportunity to further optimize MRI sessions by exploiting this shared information. On the reconstruction side, multi-contrast methods have addressed this problem by introducing the shared information into the reconstruction phase to allow higher levels of k-space undersampling. In the simplest case of two contrasts, multi-contrast reconstruction can be classified into two types – (a) guided reconstruction, where an existing high-quality reference scan is used to guide the reconstruction of an undersampled second scan (Ehrhardt and Betcke, 2016; Weizman et al., 2016; Zhou and Zhou, 2020) and (b) joint reconstruction, where both contrasts are undersampled and are reconstructed simultaneously (Bilgic et al., 2011; Huang et al., 2014; Kopanoglu et al., 2020). In this work, we consider the problem of guided reconstruction, assuming no inter-scan motion between reference and target scans.

The guided reconstruction problem entails using the local structure of the reference scan as a prior to complement the undersampled k-space measurements of the target scan. This problem has been formulated in different ways, ranging from conventional CS (Ehrhardt and Betcke, 2016; Weizman et al., 2016) to end-to-end learning with unrolled networks (Zhou and Zhou, 2020; Yang et al., 2020; Pooja et al., 2022; Lei et al., 2023) and, more recently, diffusion model-based Bayesian maximum *a posteriori* estimation (Levac et al., 2023). Most end-to-end approaches, although more powerful than earlier hand-crafted ones, suffer from the main drawback of requiring large paired training datasets consisting of the target image and its k-space together with an aligned reference image, thereby limiting their application on real-world MR data. We address this issue by proposing a plug-and-play reconstruction method that splits the problem

into a purely image-domain learning sub-problem and an iterative reconstruction sub-problem. The learning problem leverages ideas from content/style decomposition, thereby offering a degree of interpretability to our approach. To the best of our knowledge, ours is the first work that thoroughly explores content/style-based generative modeling for multi-contrast MRI reconstruction.

In recent years, image-to-image translation has found application in the direct estimation of one MR contrast from another (Dar et al., 2019; Yurt et al., 2021; Denck et al., 2021; Atli et al., 2024). While these methods are attractive due to their lack of dependence on k-space data, viewed in the light of MR physics, cross-contrast translation takes an extreme stance by not explicitly taking into account contrast-specific sensitivities and relying solely on the prior contrast. Hence, in the context of MR image formation, cross-contrast translation, by itself, can only provide a part of the information about the target image as data acquisition via MR sequences is necessary to obtain new information about the anatomy. That being said, literature on unpaired image translation provides a repertoire of useful tools such as joint generative modeling of two-domain image data (Liu et al., 2017; Huang et al., 2018), which can be adopted to complement image reconstruction. We observe that methods such as MUNIT (Huang et al., 2018) can be applied to learn semantically meaningful representations of contrast-independent and contrast-specific information as content and style, respectively, without the need for paired image-domain training data.

Plug-and-play (PnP) methods are an emerging paradigm for solving inverse problems in computational imaging. The main research line (Ahmad et al., 2020; Kamilov et al., 2023) has focused on learning CNN-based denoising models on image-domain data and applying them as functions replacing proximal operators in iterative algorithms like ISTA and ADMM, demonstrating improved image recovery. An advantage of this approach is the decoupling of the learning problem of image modeling from the inverse problem of image reconstruction, thereby simplifying model training and improving generalizability across different acceleration factors, undersampling patterns, etc. With this design pattern in mind, we combine content/style image modeling and iterative reconstruction in a PnP-like framework.

We first leverage semantic content/style modeling to learn explicit representations of contrast-independent and contrast-specific components from two-contrast MR image data. This training process is independent of the reconstruction problem and can be performed using unpaired images. We then make the interesting observation that in multi-contrast MR images, the style information tends to localize in the center of the k-space, allowing for an accurate style estimation from an undersampled image. Since the content of the reconstructing image, which is the remaining piece of information and is contrast-independent, is supplied by the reference image, one can compose a de-aliased estimate of the reconstruction from the undersampled image in a single step. We term this the *content consistency operation*, which forms the basis of our iterative reconstruction algorithm PnP-CoSMo (Plug-and-Play method based on Content/Style Modeling) (Rao et al., 2024). An overview of our approach is shown in Fig. 1. While the PnP-based decoupling of image modeling and image reconstruction simplifies the training process and allows the two stages to be analyzed separately, a further level of decoupling offered by content/style disentanglement offers additional modularity and an intuitive guidance mechanism for the reconstruction. Specifically, our contributions are four-fold:

1. We show that unpaired image-domain training can be used to learn disentangled contrast-independent and contrast-specific representations, followed by a fine-tuning strategy that refines the content representation using a modest amount of paired image-domain data.
2. With this content/style model as the basis, we define a *content consistency operator* capable of removing severe undersampling artifacts from the reconstructing image, given the corresponding reference image.
3. Developing this idea further and incorporating a corrective process for the content, we propose PnP-CoSMo, a modular algorithm for guided reconstruction combining the flexibility of the plug-and-play approach with the semantic interpretability of content/style decomposition.
4. Through comprehensive experiments, we shed light on several properties of PnP-CoSMo such as convergence and robustness and demonstrate its applicability on real-world raw data and its potential clinical utility with a specific radiological task.

2. Related work

2.1. Reconstruction methods for accelerated MRI

Techniques for accelerating MRI by k-space undersampling go back to compressed sensing (CS) (Lustig et al., 2007), which combines random sampling with sparsity-based iterative denoising, most commonly implemented based on the ISTA (Chambolle et al., 1998) or ADMM ((Boyd et al., 2011)) family of algorithms. Most modern deep learning-based reconstruction methods focus on improving the denoising part. Plug-and-play (PnP) methods (Ahmad et al., 2020; Kamilov et al., 2023) replace the cstep operator in ISTA and ADMM with off-the-shelf denoisers such as a learned convolutional denoising model. Unrolled networks (Schlemper et al., 2017; Aggarwal et al., 2018; Pezzotti et al., 2020) extend this idea by casting the entire iterative algorithm into one large network, trained end-to-end. This makes them more adaptive to factors such as sampling pattern and acceleration, although at a cost of generalizability (Ahmad et al., 2020).

One of the earliest CS-based guided reconstruction methods was proposed by Ehrhardt and Betcke (2016) introducing structure-guided total variation (STV), which assumes the sparse coefficients of the reconstruction to be partially known based on the edge features in the reference scan. Later work introduced adaptive elements into the multi-contrast CS framework, e.g. Weizman et al. (2016) proposed adaptive weighting-based guided CS and Pingfan et al. (2018) used adaptive sparse domains based on coupled dictionary learning. In the latter, the problem was formulated using a patch-level linear model comprising coupled and distinct sparse dictionary representations of the two contrasts. This model resembles a content/style model in form, although it is more restrictive. A general drawback of classical methods compared to deep learning-based ones is their lower flexibility. End-to-end learning-based methods (Zhou and Zhou, 2020; Yang et al., 2020; Liu et al., 2021a,b; Feng et al., 2022; Lei et al., 2023), on the other hand, supply the reference scan as an additional input to a deep reconstruction model allowing it to automatically learn the suitable features to extract and transfer into the reconstruction, and have proven to be more effective than conventional algorithms. However, end-to-end methods require large paired training datasets comprising the ground-truth image and the k-space together with aligned reference images, which is too strong a constraint when working with retrospectively collected clinical data that reflects the natural inconsistencies of routine practice such as missing contrasts, differences in spatial resolutions, and the existence of inter-scan motion. Additionally, by relying on end-to-end-learned features, these methods are generally less interpretable than their conventional counterparts in that they do not explicitly model the multi-contrast problem in terms of the underlying shared and non-shared information. MC-VarNet (Lei et al., 2023) is an important exception, which uses a simple linear decomposition of the reference contrast into common and unique components, applying the common component for guidance.

A reconstruction method that is as effective as the learning-based methods while having more lenient data requirements and offering a high degree of interpretability is still needed. Our plug-and-play method relies on learning a deep non-linear content/style transform from image-domain data only, even if subject-wise paired images are not fully available.

2.2. Unpaired image-to-image modeling

Image-to-image modeling is the general problem of learning a mapping between two image domains and was first addressed by Pix2Pix (Isola et al., 2017) and CycleGAN (Zhu et al., 2017) in paired and unpaired settings, respectively. Another line of unpaired image translation methods, the first of which was UNIT (Liu et al., 2017), assumes a shared latent space underlying the two domains to explicitly represent shared information. However, both CycleGAN and UNIT assume a deterministic one-to-one mapping between the two domains, ignoring the fact that an image in one domain can have multiple valid renderings in the other. Deterministic image translation has been widely applied to MRI contrast-to-contrast synthesis (Dar et al., 2019; Oh et al., 2020; Yurt et al., 2021). However, fundamentally, these methods do not account for the variability of the scanning setup that influences the realized contrast level and the differential visibility of pathologies in the target image. Denck et al. (2021) partially address this problem by proposing contrast-aware MR image translation where the acquisition sequence parameters are fed into the network to control the output’s contrast level. However, this model is too restrictive since it assumes a single pre-defined mode

of variability (i.e. global contrast level) in the data, for which the labels (i.e. sequence parameters) must be available.

MUNIT (Huang et al., 2018) extended UNIT by modeling domain-specific variability in addition to domain-independent structure, enabling many-to-many mapping and thus overcoming the rigidity of UNIT. The result was a stochastic image translation model which, given an input image, generates a distribution of synthetic images sharing the same "content" but differing in "style". More fundamentally, MUNIT is a learned invertible transformation between the image domains and the disentangled content/style domains. And unlike other content/style modeling frameworks such as (Kotovenko et al., 2019; Kwon and Ye, 2021; Wu et al., 2023), MUNIT models content and style as latent generative factors of the two image domains, providing precise distribution-level definitions for them. Clinical MR images of a given protocol contain multiple modes of variability, many of which are not known *a priori*. Compared to Denck et al. (2021), we make a broader assumption that the contrast-independent semantic information is local in nature and that the contrast-specific variations in the dataset can include global effects of acquisition settings as well as local anatomical features unique to the contrast. We model using an approach based on the MUNIT framework, referring to the shared and non-shared components as content and style, respectively.

2.3. Combining image translation with reconstruction

Acknowledging the limitation of MR cross-contrast prediction, some prior work has attempted combining it with multi-contrast reconstruction. A naive form of joint image synthesis and reconstruction, e.g. PROSIT (Mattern et al., 2020) and rsGAN (Dar et al., 2020), involves generating a synthetic image from the reference scan via deterministic image translation and using it in a classical L2-regularized least-squares reconstruction. More recent work by Xuan et al. (2022) proposed a joint image translation and reconstruction method which additionally accounts for misalignment between the reference and reconstructing images, with a follow-up work leveraging optimal transport theory (Wang et al., 2024). Levac et al. (2023) formulate guided reconstruction as a highly general Bayesian maximum *a posteriori* estimation problem and solve it iteratively via Langevin update steps, using an image-domain diffusion model as the score function of the prior distribution. While these are promising directions, we propose an alternative approach that decomposes the multi-contrast problem in a more intuitive way – first, into two sub-problems, namely image modeling and image reconstruction; and second, within the image-domain model, the multi-contrast information is decomposed into content and style. This two-level decomposition results in a highly modular reconstruction algorithm with a built-in explanatory framework where (a) the guidance mechanism is a simple content-replacement operation, (b) the discrepancy between the supplied reference content and the true content of the target image represents a meaningful error term which can be minimized, and (c) the optimal content-encoding capacity of the model for a given two-contrast image dataset indicates the amount of shared structure that is available to be learned in this data and utilized in the reconstruction task.

3. Methods

3.1. Reconstruction problem

3.1.1. Undersampled MRI reconstruction

Given a set of P acquired k-space samples $y \in \mathbb{C}^P$ and the MRI forward operator $A \in \mathbb{C}^{P \times Q}$, CS reconstruction of the image $x \in \mathbb{C}^Q$ with Q voxels is given as

$$\min_x \|Ax - y\|_2^2 + \lambda \|\Psi x\|_1, \quad (1)$$

where Ψ is some sparsifying transform (e.g. wavelet) and λ is the regularization strength. A commonly used algorithm to solve this optimization problem is ISTA, which iteratively applies the following two update steps:

$$r^k \leftarrow \Psi^H \text{soft}(\Psi x^{k-1}; \lambda), \quad (2)$$

$$x^k \leftarrow r^k - \eta A^H (Ar^k - y). \quad (3)$$

Eq. (2) performs soft-thresholding in the transform domain, thereby reducing the incoherent undersampling artifacts in image x^{k-1} , whereas (3) enforces soft data consistency on image r^k by taking a single gradient descent step over the least-squares term, controlled by step size η .

3.1.2. Plug-and-play denoiser

Plug-and-play methods replace the analytical operation of (2) with off-the-shelf denoisers. A CNN-based denoiser is of special interest as it incorporates a learning-based component into iterative reconstruction. Given a CNN model f_θ trained to remove i.i.d. Gaussian noise from an image, PnP-CNN (Ahmad et al., 2020) modifies Eq. (2) to

$$z^k \leftarrow f_\theta(x^{k-1}). \quad (4)$$

3.1.3. Plug-and-play content consistency operator

In guided reconstruction, a spatially aligned reference x_1^{ref} is available, which captures the same underlying *semantic content* as the target reconstruction. Inspired by the PnP design, we cast the problem of incorporating prior information from x_1^{ref} into the reconstruction iterate x_2^{k-1} as enforcing a hard consistency between this image iterate and its semantic content estimated from the reference. We propose a *content consistency operator* $g_M(\cdot; c)$ such that

$$z_2^k \leftarrow g_M(x_2^{k-1}; c), \quad (5)$$

where a content/style model M decomposes x_2^{k-1} into content and style, followed by a replacement of this corrupted content with high-quality content c derived from x_1^{ref} and composing the improved image z_2^k from it. Before formally defining this operator and developing the reconstruction algorithm, we discuss in the following section the design and learning of the content/style model M .

3.2. Content/Style modeling

Given an image dataset of two MR contrasts we make the general assumption that there exists an underlying contrast-independent structure which, influenced by arbitrary contrast-specific factors, is rendered as the contrast images. We formulate our content/style model based on the MUNIT framework (Huang et al., 2018).

3.2.1. Unpaired MUNIT pre-training

We define an image domain as the set \mathcal{X}_i of images of a certain contrast comprising the dataset, where $i \in \{1, 2\}$. "Content" $c \in \mathcal{C}$ is defined as the underlying contrast-independent structure and is represented as a set of feature maps, whereas "style" $s_i \in \mathcal{S}_i$ corresponds to the various modes of variability in one domain which cannot be explained by the other, e.g. global effects of acquisition settings, contrast-specific tissue features, etc., and is represented as a low-dimensional vector. MUNIT posits the existence of functions $G_i^* : \mathcal{C} \times \mathcal{S}_i \rightarrow \mathcal{X}_i$ and their inverses $E_i^* = (G_i^*)^{-1}$, and learns them jointly via unpaired training, given samples from marginal distributions $p(x_i)$. In practice, the encoder E_i is split into content encoder E_i^c and style encoder E_i^s . Thus, the content/style model is specified as $M = \{E_1^c, E_2^c, E_1^s, E_2^s, G_1, G_2\}$.

The MUNIT loss function is comprised of four terms:

$$\mathcal{L}_{\text{MUNIT}} = \mathcal{L}_{\text{GAN}} + \alpha_1 \mathcal{L}_{\text{image}}^{\text{self}} + \alpha_2 \mathcal{L}_{\text{content}}^{\text{self}} + \alpha_3 \mathcal{L}_{\text{style}}^{\text{self}}, \quad (6)$$

where

$$\begin{aligned} \mathcal{L}_{\text{GAN}} = & \mathbb{E}_{x_1 \sim p(x_1), s_2 \sim q(s_2)} [(1 - D_2(G_2(E_1^c(x_1), s_2)))^2] + \\ & \mathbb{E}_{x_2 \sim p(x_2), s_1 \sim q(s_1)} [(1 - D_1(G_1(E_2^c(x_2), s_1)))^2], \end{aligned} \quad (7)$$

$$\begin{aligned} \mathcal{L}_{\text{image}}^{\text{self}} = & \mathbb{E}_{x_1 \sim p(x_1)} [\|x_1 - G_1(E_1^c(x_1), E_1^s(x_1))\|_1] + \\ & \mathbb{E}_{x_2 \sim p(x_2)} [\|x_2 - G_2(E_2^c(x_2), E_2^s(x_2))\|_1], \end{aligned} \quad (8)$$

$$\begin{aligned} \mathcal{L}_{\text{content}}^{\text{self}} = & \mathbb{E}_{c_1 \sim p(c_1), s_2 \sim q(s_2)} [\|c_1 - E_2^c(G_2(c_1, s_2))\|_1] + \\ & \mathbb{E}_{c_2 \sim p(c_2), s_1 \sim q(s_1)} [\|c_2 - E_1^c(G_1(c_2, s_1))\|_1], \end{aligned} \quad (9)$$

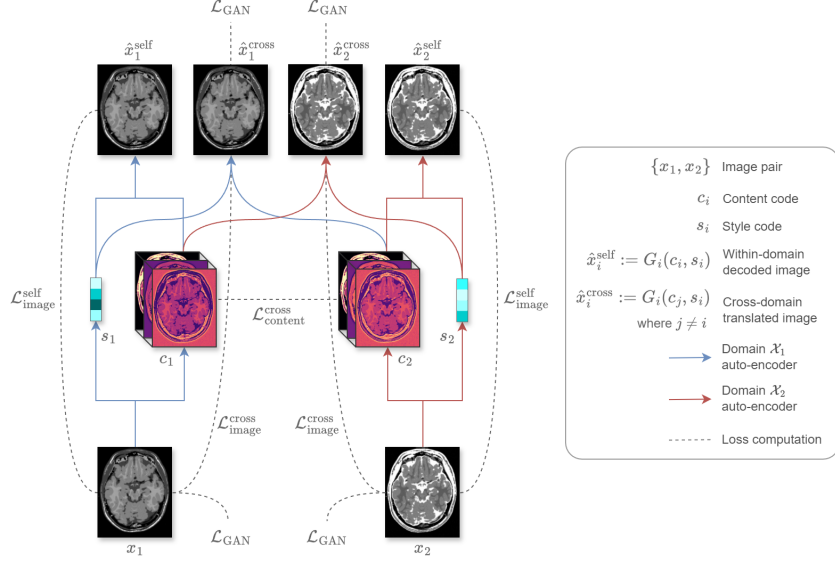


Figure 2: Our proposed paired fine-tuning (PFT) stage for improving the alignment of the content representations of the two domains given a small dataset of paired images.

$$\begin{aligned} \mathcal{L}_{\text{style}}^{\text{self}} = & \mathbb{E}_{c_1 \sim p(c_1), s_2 \sim q(s_2)} [\|s_2 - E_2^s(G_2(c_1, s_2))\|_1] + \\ & \mathbb{E}_{c_2 \sim p(c_2), s_1 \sim q(s_1)} [\|s_1 - E_1^s(G_1(c_2, s_1))\|_1]. \end{aligned} \quad (10)$$

$\mathcal{L}_{\text{image}}^{\text{self}}$ is the image recovery loss, which promotes preservation of the image information in the latent space. $\mathcal{L}_{\text{content}}^{\text{self}}$ and $\mathcal{L}_{\text{style}}^{\text{self}}$ are the content and style recovery losses, respectively, which specialize parts of the latent code into content and style components. \mathcal{L}_{GAN} is the adversarial loss, which enables unpaired training by enforcing distribution-level similarity between synthetic and real images via discriminators D_1 and D_2 . α_1 , α_2 , and α_3 are hyperparameters. For our purpose, we consider the MUNIT training process as the pre-training stage of our content/style model.

3.2.2. Paired fine-tuning

While the pre-training stage learns useful content/style representations, we adapt the model to our task by improving its content preservation. To this end, we propose a paired fine-tuning (PFT) stage which more strongly aligns the content representations of the two domains given a modest amount of paired data. Given samples from the joint distribution $p(x_1, x_2)$, our fine-tuning objective is expressed as

$$\mathcal{L}_{\text{PFT}} = \mathcal{L}_{\text{GAN}} + \beta_1 \mathcal{L}_{\text{image}}^{\text{self}} + \beta_2 \mathcal{L}_{\text{image}}^{\text{cross}} + \beta_3 \mathcal{L}_{\text{content}}^{\text{cross}}, \quad (11)$$

where

$$\begin{aligned} \mathcal{L}_{\text{image}}^{\text{cross}} = & \mathbb{E}_{\{x_1, x_2\} \sim p(x_1, x_2)} [\|x_2 - G_2(E_1^c(x_1), E_2^s(x_2))\|_1 + \\ & \|x_1 - G_1(E_2^c(x_2), E_1^s(x_1))\|_1], \end{aligned} \quad (12)$$

$$\mathcal{L}_{\text{content}}^{\text{cross}} = \mathbb{E}_{\{x_1, x_2\} \sim p(x_1, x_2)} [\|E_1^c(x_1) - E_2^c(x_2)\|_1]. \quad (13)$$

$\mathcal{L}_{\text{image}}^{\text{cross}}$ is a pixel-wise image translation loss, which provides image-level supervision, and $\mathcal{L}_{\text{content}}^{\text{cross}}$ is a paired content loss, which penalizes discrepancy between the contents. β_1 , β_2 , and β_3 are an additional set of hyperparameters. Note that our PFT preserves the bi-directionality of the content/style model, a property which will later be essential for generalization over different reconstruction tasks.

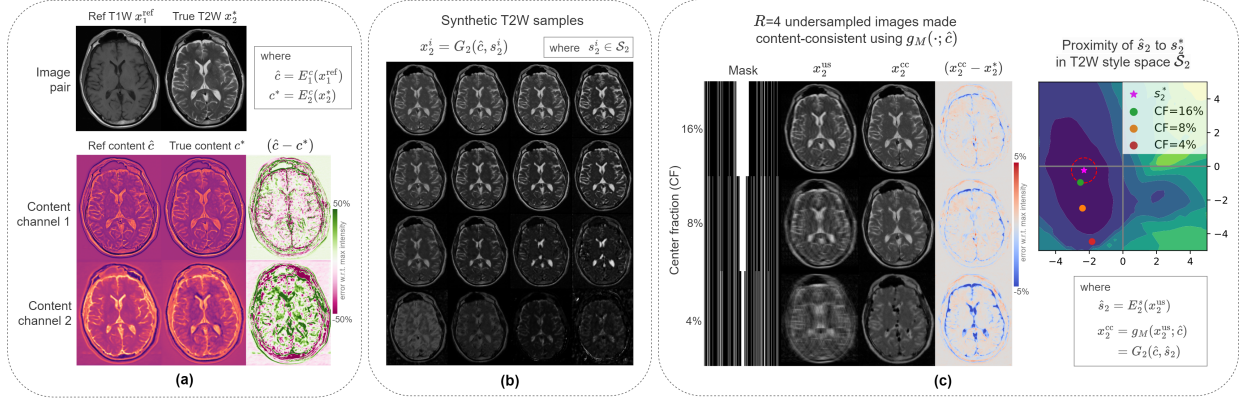


Figure 3: Demonstration of the content consistency operator $g_M(\cdot; c)$ based on a content/style model M . The image pair shown here are NYU brain DICOMs, practical details regarding which are provided in Section 4. (a) A T1W/T2W image pair and the corresponding content maps. While these two content maps generally agree, there is a notable discrepancy. (b) Synthetic T2W images generated from 16 style codes grid-sampled from \mathcal{S}_2 , showing a smooth variation in image contrast and a roughly constant anatomical structure. (c) $g_M(\cdot; c)$ is applied on 3 cases where x_2^* was corrupted with $R=4$ undersampling with different center fractions. Sampling more low-frequency lines leads to more accurate style estimate \hat{s}_2 and thus a better image x_2^{cc} . Contours in \mathcal{S}_2 indicate the MAE of the synthetic images from that region. The red circle indicates a style estimation NMSE of 0.1.

3.2.3. Network architecture and content capacity

Following the original MUNIT paper (Huang et al., 2018), our content encoders E_i^c consist of an input convolutional layer potentially followed by strided downsampling convolutions, and finally a series of residual blocks. Style encoders E_i^s consist of input and downsampling convolutions followed by adaptive average pooling and a fully-connected layer that outputs the latent vector. Decoders G_i follow a similar structure as the content encoders except in reverse. Style is introduced into the decoder via AdaIN operations which modulate the activation maps derived from the content. We observe that in this architecture, the ratio between the content resolution and the image resolution reflects the level of local structure one expects to be shared between the two domains. This (relative) content resolution is thus an inductive bias built into the model, which we refer to as the model’s *content capacity* and define as

$$J_M := \frac{H_c W_c}{H_x W_x}, \quad (14)$$

where H_x and W_x are the height and width of the input image and $H_c (\leq H_x)$ and $W_c (\leq W_x)$ are the those of the corresponding content maps. This ratio is controlled via the number of up/downsampling blocks in the networks. Our notion of content capacity is closely related to the more general concept of the locality bias of image-to-image models (Richardson and Weiss, 2021). A content/style model with a high content capacity has a large content resolution, allowing it to learn a rich, highly expressive content representation that strongly influences the output’s structure. Consequently, the model’s style spaces are restricted to learn mostly low-level global features.

3.3. Iterative reconstruction based on content consistency

Given the content/style model M , we consider \mathcal{X}_1 and \mathcal{X}_2 as reference and target domains, respectively, in our guided reconstruction task, and define the content consistency operator $g_M(\cdot; c)$ from Eq. (5) as

$$x_2^{\text{cc}} = g_M(x_2^{\text{us}}; \hat{c}) := G_2(\hat{c}, E_2^s(x_2^{\text{us}})), \quad (15)$$

where x_2^{us} is the image containing undersampling artifacts, x_2^{cc} is the content-consistent image, and $\hat{c} = E_1^c(x_1^{\text{ref}})$ is the reference content. This operation improves x_2^{us} by simply replacing its aliased content with the content estimated from x_1^{ref} , a rule which will later be softened with (17).

Note that this is a radical operation as it discards all structure contained in x_2^{us} , retaining only a compact style code $\hat{s}_2 = E_2^s(x_2^{\text{us}})$. Let x_2^* be the ground truth reconstruction with content c^* and style s_2^* . The success of our content consistency operation depends on three conditions – (a) \hat{c} and c^* are rich, high-resolution representations of the underlying anatomy, (b) \hat{c} is close to c^* , and (c) \hat{s}_2 is close to s_2^* . The first condition is satisfied provided that there is sufficient amount of shared structure between the reference and target domains and that the model has high content capacity J_M for capturing a highly expressive content. The second condition is roughly satisfied, as seen in Fig. 3a, because the model is explicitly trained to minimize content error, but more on this later. On the other hand, it is not obvious that the third condition should hold too and it hence deserves a closer look. If the first condition is satisfied, the optimal model will have a high content capacity and consequently, style would represent mostly low-level global image features, e.g. contrast variations (see Section 3.2.3). This is observed in practice as shown in Fig. 3b. It is a well known fact that image contrast is contained prominently in the center of the k-space. Hence, the estimate \hat{s}_2 can be made arbitrarily close to s_2^* by sufficiently sampling the k-space center, as demonstrated empirically in Fig. 3c.

Applying data consistency update (3) following $g_M(\cdot; \hat{c})$ in repetition yields an ISTA-based iterative scheme. Here, our content consistency update complements the data consistency update in the sense that while the latter forces the image estimate to be consistent with the given (measured) k-space data y , the former forces it to be consistent with the given (prior) content \hat{c} .

Algorithm 1 PnP-CoSMo iterative guided reconstruction

Require: $y, A, x_1^{\text{ref}}, M, \eta, \gamma$ ▷ where $M = \{E_1^c, E_1^s, E_2^c, E_2^s, G_1, G_2\}$
1: $k \leftarrow 0$
2: $x_2^k \leftarrow A^H y$ ▷ Initialize reconstruction
3: $c^k \leftarrow E_1^c(x_1^{\text{ref}})$ ▷ Initialize content
4: **repeat**
5: $k \leftarrow k + 1$
6: $z_2^k \leftarrow g_M(x_2^{k-1}; c^{k-1})$ ▷ Content consistency update
7: $x_2^k \leftarrow z_2^k - \eta A^H (A z_2^k - y)$ ▷ Data consistency update
8: $c^k \leftarrow c^{k-1} - \gamma \nabla_c \|AG_2(c^{k-1}, E_2^s(x_2^k)) - y\|_2^2$ ▷ Content refinement (CR) update
9: **until** convergence
10: **return** x_2^k

The core assumption of an idealized content/style model is that contents \hat{c} and c^* are identical. However, in reality, this assumption will not hold, and a discrepancy between the two contents is to be expected. There are two possible sources of this discrepancy – (a) model-related, e.g. fundamental limits such as irreducible error¹ and practical issues like sub-optimal network design and training, and (b) reference image-related, e.g. presence of artifacts independent of the target reconstruction. We refer to this gap between \hat{c} and c^* as *content discrepancy*. Fig.3a shows content discrepancy as observed empirically. During reconstruction, the error in \hat{c} would limit the efficacy of the operator $g_M(\cdot; \hat{c})$, affecting the reconstruction quality. While model-related discrepancy is partly tackled by PFT (Section 3.2.2), we now propose a *content refinement* (CR) process to correct for the remaining discrepancy in the reconstruction stage. Since we have no direct access to the true content c^* , but only to undersampled k-space measurements y , we aim at solving the following minimization problem in CR

$$\min_c \|AG_2(c, \hat{s}_2) - y\|_2^2, \quad (16)$$

starting from the initial point $\hat{c} = E_1^c(x_1^{\text{ref}})$ and for a given style estimate \hat{s}_2 . The augmented forward operator $AG_2(\cdot)$ is a composition of the linear MRI forward operator A and the non-linear content/style

¹If perfectly zero error was possible, one could perfectly predict the (distribution of) target image from the reference without any measurement.

decoder G_2 , and it maps the content domain to the k-space domain. The error between the predicted k-space $AG_2(c, \hat{s}_2)$ and the measured data y serves as a proxy for content discrepancy, which can be computed and minimized during the reconstruction. We approximate the solution with a single gradient descent step

$$c^k \leftarrow c^{k-1} - \gamma \nabla_c \|AG_2(c^{k-1}, \hat{s}_2^k) - y\|_2^2, \quad (17)$$

initialized as $c^0 \leftarrow E_1^c(x_1^{\text{ref}})$ and updated every k^{th} iteration with step size γ following the data consistency and content consistency updates. Hence, by aligning the content c with k-space data y and correcting the discrepancy, the CR module aligns content consistency updates with data consistency updates. With this additional component in place, we obtain our PnP-CoSMo reconstruction algorithm (Algorithm 1). Note that unlike content, the style of the image estimate need not be explicitly aligned with the k-space. Since the style information is assumed to be derived largely from the k-space data, the data consistency update applied on the image implicitly "corrects" its style. Thus, as the image converges, we hypothesize that style would converge as well.

4. Experimental setup

4.1. Experiment design

We conducted 4 sets of experiments to comprehensively evaluate PnP-CoSMo – (a) simulations, (b) benchmark against end-to-end methods on NYU DICOM data, (c) benchmark and ablation on clinical multi-coil raw data, and (d) radiological evaluation. Without loss of generality, we considered the case of reconstructing T2W scans using T1W references and focused on head applications, except in the NYU benchmark where the reverse case was considered as well.

4.1.1. Simulation

The goal of our simulation experiments was to empirically test several properties of our algorithm under highly controlled settings. To this end, we used simulated T1W and T2W images based on BrainWeb phantoms (Collins et al., 1998). BrainWeb provides 20 anatomical models of normal brain, each comprised of fuzzy segmentation maps of 12 tissue types. The 20 volumes were first split into the model training (18), model validation (1), and reconstruction testing (1) subsets. T1W/T2W spin-echo scans were simulated using TE/TR values randomly sampled from realistic ranges. For testing the reconstruction, 2D single-coil T2W k-space data was simulated via Fourier transform and 1D Cartesian random sampling at various accelerations. We analyzed the effect of the content/style model’s disentanglement level and its content capacity on the reconstruction quality, the convergence of the PnP-CoSMo algorithm, and the effectiveness, robustness, and tuning of the CR module.

4.1.2. Benchmark on the NYU DICOM dataset

In the NYU benchmark, we compared PnP-CoSMo against end-to-end reconstruction methods. The question we sought to answer was whether or not PnP-CoSMo, which requires only image-domain training data, can outperform methods that additionally require k-space training data. Furthermore, end-to-end methods are task-specific where the reference and target contrast are fixed – e.g. T1W and T2W, respectively. On the other hand, the content/style model used in PnP-CoSMo does not possess this kind of uni-directionality. Hence, we sought to assess the generalizability of PnP-CoSMo across two different reconstruction tasks, namely T1W-guided T2W reconstruction and T2W-guided T1W reconstruction. The NYU brain dataset (Knoll et al., 2020; Zbontar et al., 1811) includes raw data and DICOM scans of 4 contrasts – T1W with and without gadolinium agent, T2W, and FLAIR. For multi-contrast experiments, however, the NYU raw dataset does not provide subject labels for pairing the contrasts. Therefore, instead of the NYU raw data, we used the NYU DICOMs in this study, following Xuan et al. (2022). A paired DICOM subset of 327 subjects was obtained based on T2W and non-gadolinium T1W scans. All T1W scans were rigid-registered with the corresponding T2W scans. Single-coil k-space data was simulated via Fourier transform with 1D Cartesian random sampling at $R \in \{2, 3, 4, 5\}$ and added Gaussian noise of $\sigma = 0.01 \max(x_2^*)$. The dataset was split into 4 subsets – *model-train* (200), *model-val* (27), *recon-val* (50), and *recon-test* (50). Images from

Table 1: Overview of the sequences in the LUMC datasets.

Sequence Params	LUMC-TRA			LUMC-COR		
	3D T1W TFE	2D T2W TSE	3D T1W TSE	2D T2W TSE		
FA (deg)	8	90	80-90	90		
TR (ms)	9.8-9.9	4000-5000	500-800	2000-3500		
TE (ms)	4.6	80-100	6.5-16	90-100		
ETL	200	14-18	10-13	17-19		
Voxel size (mm)	0.98×0.99 ×0.91	0.4×0.54	0.59×0.62 ×1.19	0.39×0.47		
Slice thick. (mm)	–	3	–	2		
FOV (mm)	238×191 ×218	238×190	130×238 ×38	130×197		
Num slices	–	50	–	15		

Table 2: LUMC data split. The splits were made at the subject-level, i.e. each subject belonged to exactly one subset. Splits containing only image-domain data are marked with \mathcal{T} . The *recon-val* and *recon-test* splits additionally include raw T2W multi-coil k-space and coil sensitivities.

Dataset	Split	Subjects	Sessions	Scans (T1W / T2W)
LUMC-TRA	<i>model-train</i> \mathcal{T}	295	418	360 / 415
	<i>model-val</i> \mathcal{T}	16	17	17 / 17
	<i>recon-val</i>	18	21	21 / 21
	<i>recon-test</i>	20	31	31 / 31
	Total	339	487	429 / 484
LUMC-COR	<i>model-train</i> \mathcal{T}	242	277	269 / 272
	<i>model-val</i> \mathcal{T}	18	18	18 / 18
	<i>recon-val</i>	15	18	18 / 18
	<i>recon-test</i>	16	17	17 / 17
	Total	291	330	322 / 325

the former two splits were used to pre-train, fine-tune, and validate the content/style model. End-to-end models were trained and validated on the aligned T1W, the simulated T2W k-space, and the T2W ground-truth from these two splits. The *recon-val* split was used to tune the PnP-CoSMo algorithm, and *recon-test* was the held-out test set. We benchmarked PnP-CoSMo against one well-known single-contrast network – MoDL (Aggarwal et al., 2018) – and two recent multi-contrast networks – MTrans (Feng et al., 2022) and MC-VarNet (Lei et al., 2023). These networks were evaluated on the aforementioned two reconstruction tasks, assessing both their in-distribution and out-of-distribution performance – e.g. for the T1W-guided T2W reconstruction task, in-distribution means that the end-to-end model was trained on this task, whereas out-of-distribution means the model was trained of the T2W-guided T1W reconstruction task.

4.1.3. Benchmark and ablation on the LUMC multi-coil dataset

In our benchmark on clinical multi-coil data, the goal was to test PnP-CoSMo on a constrained real-world problem where only the image-domain data was available for training. This is often the case, as in clinical practice raw data is discarded after acquisition and only the final reconstructions are retained. Moreover, the T1W/T2W images were not fully subject-wise paired, representing a realistic case of data imbalance. Our in-house data consisted of brain scans of patients from LUMC, the use of which was approved for research purpose by the institutional review board. A total of 1669 brain scans were obtained from 817 clinical MR examinations of 630 patients acquired on 3T Philips Ingenia scanners. We focused on accelerating two T2W sequences – (a) 2D T2W TSE transversal and (b) 2D T2W TSE coronal. For guidance, two corresponding T1W sequences were used – (a) 3D T1W TFE transversal and (b) 3D T1W TSE coronal. The transversal and coronal protocols were considered as two separate datasets, namely LUMC-TRA and LUMC-COR.

Table 1 shows an overview of the four sequences. Note that the in-plane resolution of the T1W scans was 1.3-2.5 times as low as that of the T2W scans, making these datasets more challenging for T1W-guided T2W reconstruction.

As with the NYU dataset, the LUMC datasets were split into *model-train*, *model-val*, *recon-val*, and *recon-test*. The former two splits contained only image-domain data, which was used to train and validate the content/style models. The models were pre-trained on the full *model-train* splits, ignoring any pairing between T1W and T2W scans. Additionally, 20 subjects from the *model-train* split were designated for PFT where the pairing information was used in training and the reference scans were aligned via registration. The *recon-val* and *recon-test* splits additionally included multi-coil T2W raw data, which comprised 6-channel (LUMC-TRA) and 13-channel (LUMC-COR) k-space and coil sensitivity maps. This k-space was already undersampled (1D Cartesian random) at acquisition with clinical acceleration of $R=1.8-2$. We further undersampled it retrospectively to higher accelerations $R \in \{4, 6, 8, 10\}$ by dropping subsets of the acquired lines. An overview of the data split is shown in Table 2. Spatially aligned images required by all but the unpaired training set were obtained via rigid registration and the reference T1W images were resampled to the T2W resolution. During unpaired training, all images were resampled to the median T2W resolution.

Given the absence of k-space training data, end-to-end reconstruction methods were not feasible as baselines. Hence, we compared PnP-CoSMo with only the feasible types of baselines, i.e. classical, semi-classical, and plug-and-play reconstruction and image-to-image translation. Among classical methods, we used the unguided L1-wavelet CS (CS-WT) and the guided STV-based CS (CS-STV) (Ehrhardt and Betcke, 2016). As an unguided plug-and-play baseline, we used PnP-CNN (Ahmad et al., 2020), and as a representative image translation baseline, we compared against MUNIT itself. Using MUNIT, deterministic image translation was approximated by combining the reference content with 200 randomly sampled T2W style codes and taking a pixel-wise mean of the resulting synthetic images to obtain a single synthetic image. As semi-classical guided baseline, we used (PROSIT) (Mattern et al., 2020), which combines deterministic image translation with L2-regularized least-squares reconstruction. Additionally, as an ablation study for PnP-CoSMo, we ablated PFT and CR to assess their contribution, and finally, as an upperbound for PnP-CoSMo representing zero content discrepancy, we disabled PFT and CR and used the ideal content c^* . In both NYU and LUMC benchmarks, we used three perceptual metrics for evaluation – SSIM, HaarPSI, and DISTS. While SSIM is used commonly, HaarPSI and DISTS are known to correlate better with visual judgment of image quality (Kasturyulin et al., 2023). All three metrics are bounded in $[0, 1]$ where 1 represents perfect image quality. We conducted paired Wilcoxon signed-rank tests to measure statistical significance when comparing pairs of algorithms.

4.1.4. Radiological evaluation

Finally, as an extension to the LUMC benchmark, we conducted a radiological evaluation assessing the visual and diagnostic quality of PnP-CoSMo reconstructions. The study was conducted on a small sample of the LUMC-TRA *recon-test* set. With the help of a junior radiologist, we selected 3 cases with brain metastases. The evaluation was performed by a senior neuroradiologist and comprised two sets of criteria, namely visual quality and pathology. Four visual quality criteria were used, namely sharpness, noise, artifacts, and contrast between gray and white matter and CSF. For pathology, we used three criteria, namely the number and sharpness of hyperintense areas within or surrounding metastases and the overall diagnostic quality of the scan for brain metastases. The images were scored using a five-point Likert scale (Mason et al., 2019) – (1) non-diagnostic, (2) poor, (3) fair, (4) good, and (5) excellent diagnostic quality. A diagnostic-quality reconstruction was defined as one that scored at least "fairly diagnostic" on the overall diagnostic quality criterion. We evaluated PnP-CoSMo and PnP-CNN at 4 clinically realistic accelerations of $R \in \{3, 4, 5, 6\}$. In total, 9 images per patient, including the ($4 \times 2 = 8$) reconstructions and the clinical ground truth (acquired at $R=2$ and reconstructed by the vendor software), were presented to the senior neuroradiologist who scored each image individually, blinded to the reconstruction method and R .

4.2. Implementation details

We used the same general residual architecture for MUNIT encoders and decoders as the original paper, except with an additional layer at the end of the content encoder to produce content maps of specifies number

Table 3: Reconstruction PSNR (dB) over the BrainWeb test volume (300 slices). PSNR worse than the conventional L1-wavelet CS reconstruction is marked as \dagger .

Disentanglement Strength	R=2	R=4
$\alpha_2 = \alpha_3 = 10$	$15.14 \pm 0.06^\dagger$	$12.84 \pm 0.05^\dagger$
$\alpha_2 = \alpha_3 = 1$	28.43 ± 0.07	26.13 ± 0.07
$\alpha_2 = \alpha_3 = 0.1$	29.84 ± 0.05	27.33 ± 0.05
$\alpha_2 = \alpha_3 = 0.01$	25.34 ± 0.06	23.03 ± 0.05
$\alpha_2 = \alpha_3 = 0.001$	$18.17 \pm 0.07^\dagger$	$15.88 \pm 0.05^\dagger$

Table 4: Reconstruction PSNR (dB) over the BrainWeb test volume (300 slices) at $R=4$. Optimal content capacity is shown in bold. PSNR worse than the conventional L1-wavelet CS reconstruction is marked as \dagger .

Model Config	Data Config			
	RefRes-1	RefRes-1/2	RefRes-1/4	RefRes-1/8
$J_M=1$	27.90 ± 0.08	21.17 ± 0.05	19.11 ± 0.07	$16.43 \pm 0.07^\dagger$
$J_M=(1/2)^2$	26.19 ± 0.08	22.80 ± 0.08	20.05 ± 0.08	$16.57 \pm 0.08^\dagger$
$J_M=(1/4)^2$	23.98 ± 0.08	20.88 ± 0.10	19.44 ± 0.09	16.88 ± 0.06

of channels. We used 2 or 4 channels, depending on the content downsampling factor. The discriminators were implemented as multi-scale PatchGAN networks enabling them to locally assess the input images for realism at different scales. We used 1 scale in the BrainWeb simulations and 3 scales in the NYU and LUMC benchmark. We additionally conditioned the discriminators on foreground masks of the images to penalize background signal. To stabilize GAN training, we used spectral normalization (Miyato et al., 2018). For hyperparameters, we found that pre-training loss weight values $\alpha_1 = \alpha_2 = \alpha_3 = 1$ and paired fine-tuning values $\beta_1 = \beta_2 = \beta_3 = 1$ worked generally well for the *in vivo* datasets. In the benchmarks, the step size γ of the CR module of PnP-CoSMo was tuned per acceleration for each dataset and the number of iterations was set to 200.

In the simulations, all content/style models were pre-trained for 200k and were not fine-tuned for the sake of simplicity, unless stated otherwise in Section 5.1. In both NYU and LUMC benchmarks, the content/style models were pre-trained for 400k iterations and fine-tuned for 50k iterations. All software was implemented in PyTorch, and image registration was performed using Elastix (Klein et al., 2009). All training runs were performed on a compute node with an NVIDIA Quadro RTX 6000 GPU.

5. Results

5.1. Experiments on simulated MR datasets

5.1.1. Perturbation of disentanglement strength

PnP-CoSMo assumes that the content and style aspects of the images are sufficiently disentangled. Here, we evaluated the effect of perturbing the disentanglement loss weights α_2 and α_3 (Eq. (6)) of MUNIT on the PnP-CoSMo reconstruction quality. Table 3 shows the reconstruction PSNR for different weight values. We observed that optimal disentanglement, and thus the best reconstruction, was achieved at $\alpha_2 = \alpha_3 = 0.1$. At lower values, poor disentanglement of content and style in the model resulted in poor PnP-CoSMo reconstruction quality. This was expected since PnP-CoSMo relies on the assumption that the content representation is (sufficiently) contrast-independent, which was less enforced at these levels. At higher values, the training over-emphasized disentanglement while under-emphasizing the GAN and image recovery loss terms, thereby leading to worse preservation of image information in the latent space and thus, to worse reconstructions.

5.1.2. Content capacity analysis

PnP-CoSMo relies on a reference image of sufficiently high resolution to provide guidance to the reconstruction. The goal of this experiment was to determine the effect of lowering the reference image resolution on the reconstruction quality and using the content/style model’s content capacity (Eq. (14)) to explain

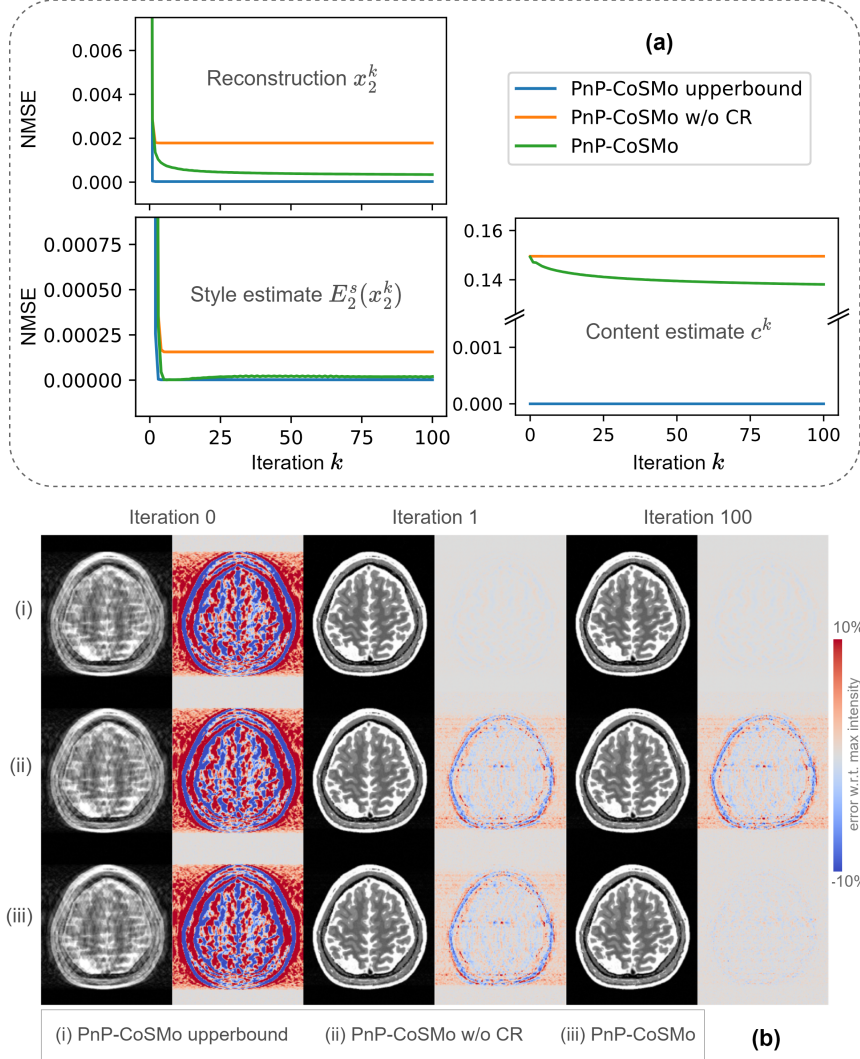


Figure 4: (a) Convergence of PnP-CoSMo and its two variants at $R=2$. (b) Evolution of the reconstruction shown with the corresponding error map.

this effect. We simulated 4 datasets, denoted as RefRes-1/ n , where $n \in \{1, 2, 4, 8\}$ represents the reference domain downsampling factor. In the $n=1$ case, the T1W/T2W images had the same resolution (as that of the underlying tissue maps), whereas in the subsequent cases, T1W images were blurred to contain only the lower $1/n$ frequency components, while maintaining the same spatial resolution. For each dataset, we trained 3 content/style models with content capacity $J_M=(1/m)^2$, where $m \in \{1, 2, 4\}$ is the content downsampling factor, which depends on the number of up/downsampling blocks in the networks. E.g. the $J_M=(1/2)^2$ model produced content maps half the spatial resolution of the $J_M=1$ model.

Table 4 compares PnP-CoSMo reconstruction quality across these configurations. PFT and CR were disabled here for simplicity. We observe two trends. First, the reconstruction quality generally decreases from left to right, eventually dropping below the conventional L1-wavelet CS reconstruction, suggesting a decrease in the amount of shared local information contained in the reference contrast. Second, the *optimal content capacity* of the model decreases with the reference resolution in accordance with the actual amount of this shared information. In other words, this optimal content capacity corresponds to the amount of contrast-independent structure the model discovers in the dataset, e.g. RefRes-1 dataset had 4 times as

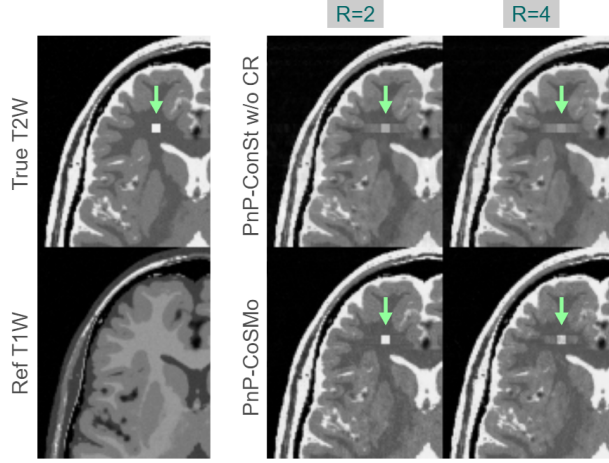


Figure 5: Effectiveness of the CR module in resolving contrast-specific structure, which, in this case, was a simulated lesion.

much shared structure (due to twice as large optimal content resolution) as RefRes-1/2 and RefRes-1/4 datasets and hence, the RefRes-1 dataset was significantly more effective in guided reconstruction. On the other hand, RefRes-1/2 and RefRes-1/4 datasets had similar levels of shared structure (i.e. $J_M=1/2^2=1/4$ times the full-resolution case) despite the lower reference resolution in RefRes-1/4, suggesting a more complex relationship between the reference resolution and the shared content. In the RefRes-1/8 case, PnP-CoSMo dropped to a similar level of quality as conventional CS, suggesting a lowerbound on the amount of shared information for PnP-CoSMo to be effective, specifically $J_M=1/4^2=1/16$ times the local information of the full-resolution case.

5.1.3. Convergence

We explored the convergence of PnP-CoSMo by comparing it with two variants. The first used true content c^* of the ground truth T2W image, thus assuming zero content discrepancy and representing an upperbound of PnP-CoSMo. The second used reference content \hat{c} with CR module disabled, representing a lowerbound of PnP-CoSMo where the non-zero content discrepancy is not corrected. Here and in the following simulation experiments, we used the RefRes-1 dataset and the $J_M=1$ model which was additionally fine-tuned on 2 training volumes for 50k iterations. Fig. 4 shows the convergence curves and intermediate reconstructions. The upperbound version, given c^* , converged in a single iteration, while with \hat{c} , the ablated version converged equally fast but to a sub-optimal solution. Enabling the CR module closed the gap with the upperbound, although at the cost of slower convergence. It is also observed that the content discrepancy reduced when using CR and that the style estimate always converged within the first few iterations, as we hypothesized in Section 3.3.

5.1.4. Effectiveness in resolving contrast-specific structure

In order to test the effectiveness of the CR module in resolving structure present in the target contrast but absent in the reference contrast, we simulated a lesion in the T2W image and performed reconstruction with and without the CR module. As shown in Fig. 5, the CR module was able to recover the lesion fully at $R=2$ and substantially at $R=4$.

5.1.5. Sensitivity to misalignment of the reference

While PnP-CoSMo expects an aligned reference image at reconstruction time, the CR module should, in principle, correct for small misalignments. To test this, we simulated a 2° rotation in the reference image and performed reconstruction at $R=4$ with and without the CR module, comparing also with PnP-CoSMo that used an aligned reference image. As shown in Fig. 6, although the reconstruction was sensitive to the misalignment in the absence of CR, it significantly improved with CR enabled.

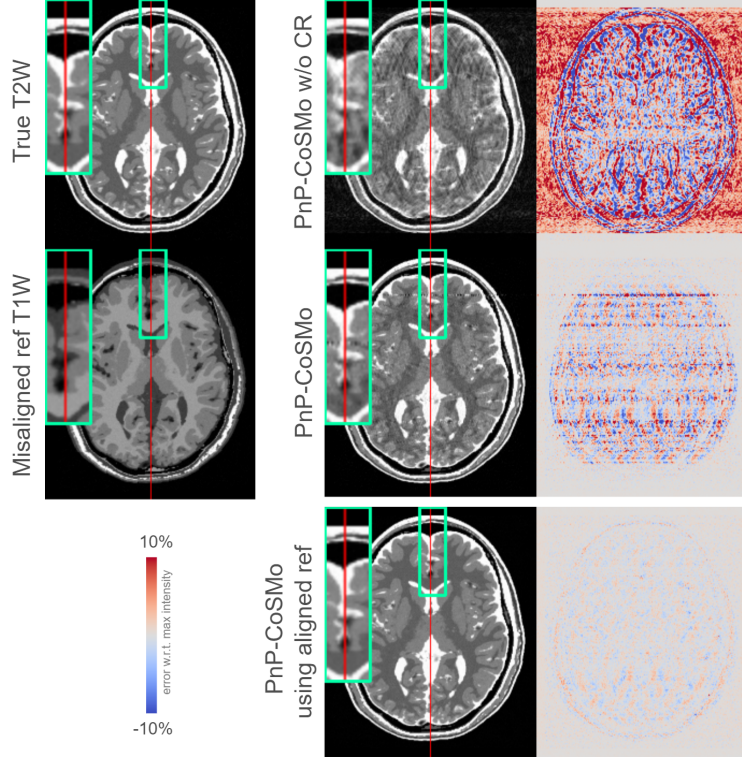


Figure 6: A misaligned reference image severely affects the reconstruction when CR is disabled. Enabling CR makes the reconstruction process robust to small misalignments.

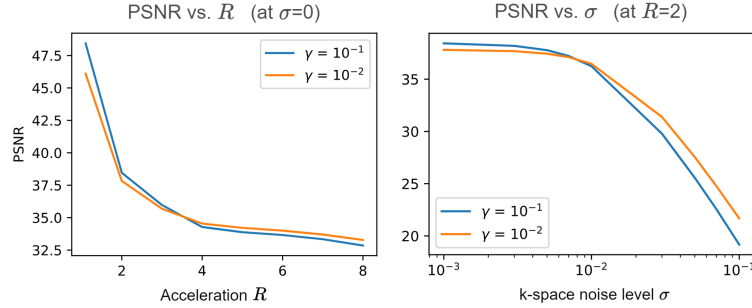


Figure 7: Reconstruction PSNR as a function of acceleration R and k-space noise level σ for different values of the hyperparameter γ . γ is the CR step size controlling the consistency of the content with the measured k-space.

5.1.6. Influence of the CR step size

The hyperparameter γ in Algorithm 1 controls the CR step size. Fig. 7 shows reconstruction quality as a function of acceleration and k-space noise level, where we observe that the optimal γ decreased with the amount and quality of k-space data. This makes sense as enforcing agreement with the k-space gradually becomes less beneficial, thereby contributing less to reconstruction quality.

5.2. Benchmark on the NYU DICOM data

In the NYU benchmarking setup considered here, let the T1W-guided T2W reconstruction task be denoted as Task-1 and the T2W-guided T1W reconstruction task as Task-2. Fig. 8 shows evaluation metrics for PnP-CoSMo and the end-to-end baselines on these two tasks. We observe three main trends. First, the

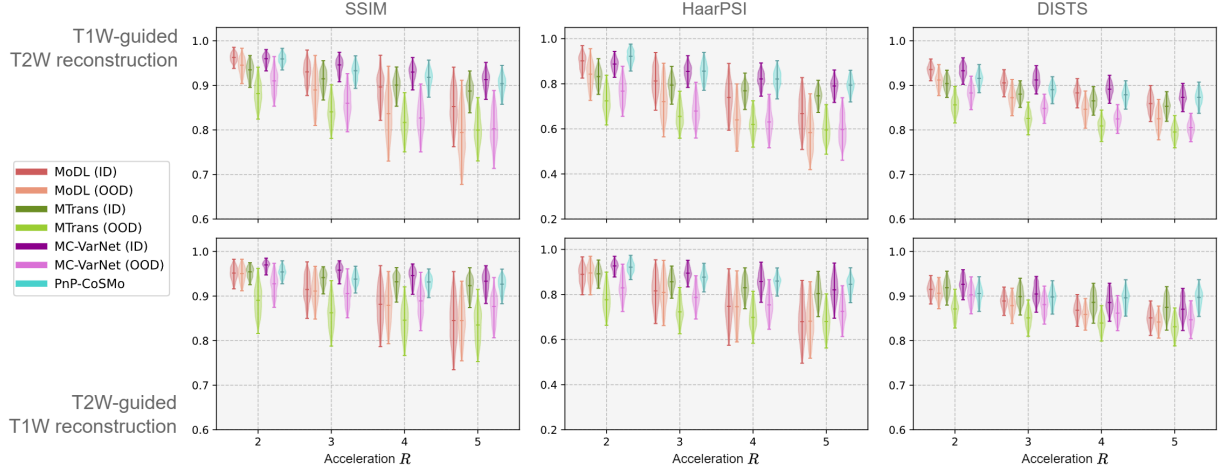


Figure 8: Evaluation plots over *recon-test* subset of NYU DICOM dataset consisting of 550 slices for the two reconstruction tasks. ID and OOD refer to in-distribution and out-of-distribution models, respectively. Note that MoDL is a single-contrast baseline and hence did not use any reference images. Unlike other methods, PnP-CoSMo, by design, required only a single content/style model for both tasks.

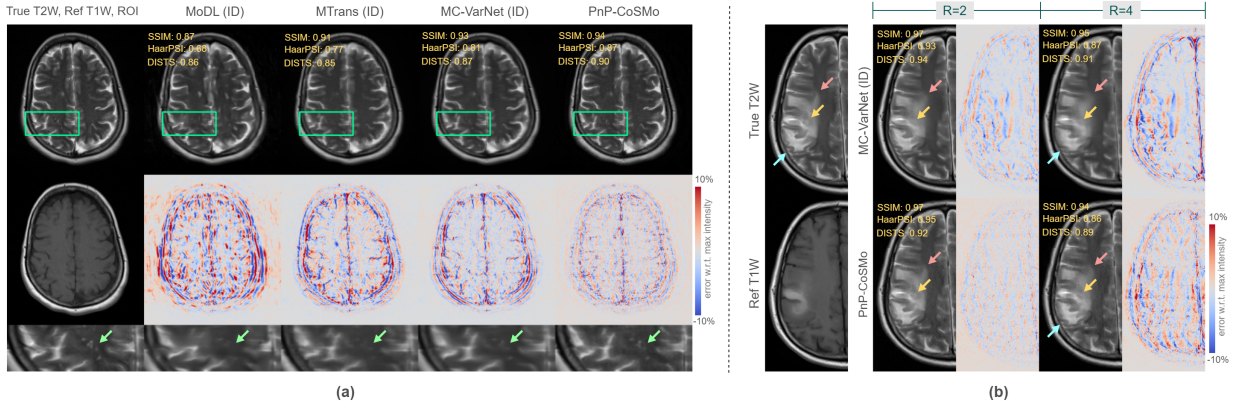


Figure 9: Two examples from the NYU benchmark for Task-1 (i.e. T1W-guided T2W reconstruction). (a) Comparison of PnP-CoSMo with the in-distribution end-to-end models at the highest acceleration of $R=5$. (b) Comparison between PnP-CoSMo and MC-VarNet at $R=2$ and $R=4$ on a pathological case where many features of the edema are T2W contrast-specific.

end-to-end methods generally dropped in performance in the out-of-distribution cases ($p < 0.05$ throughout, with the exception of SSIM at $R=5$ and HaarPsi at $R \in \{2, 4, 5\}$ for MoDL on Task-2). Second, PnP-CoSMo outperformed out-of-distribution models ($p < 0.05$, except DISTS of MoDL and MCVarNet at $R=2$ on Task-2). Since PnP-CoSMo does not depend on any task-specific k-space training data owing to both its plug-and-play design and because of the bi-directionality of the content/style model it uses, it is not susceptible to the distribution shift of this kind. Third, considering the in-distribution model performance, PnP-CoSMo largely outperformed MoDL ($p < 0.05$ throughout, except SSIM at $R=2$ and DISTS at $R \in \{2, 3, 4\}$ on Task-1 and DISTS at $R=2$ on Task-2) and MTrans ($p < 0.05$ throughout, except SSIM at $R \in \{3, 4\}$ and DISTS at $R \in \{2, 3\}$), and was roughly comparable to MC-VarNet, despite having lenient training data requirements. As shown in Fig. 9a, PnP-CoSMo could resolve certain fine details even at the high acceleration of $R=5$, which the baselines failed at. In the pathological case shown in Fig. 9b, PnP-CoSMo produced sharper reconstructions while preserving the structure of the edema better than (the in-distribution) MC-VarNet, despite lower metrics, when many features of edema were absent in the reference image.

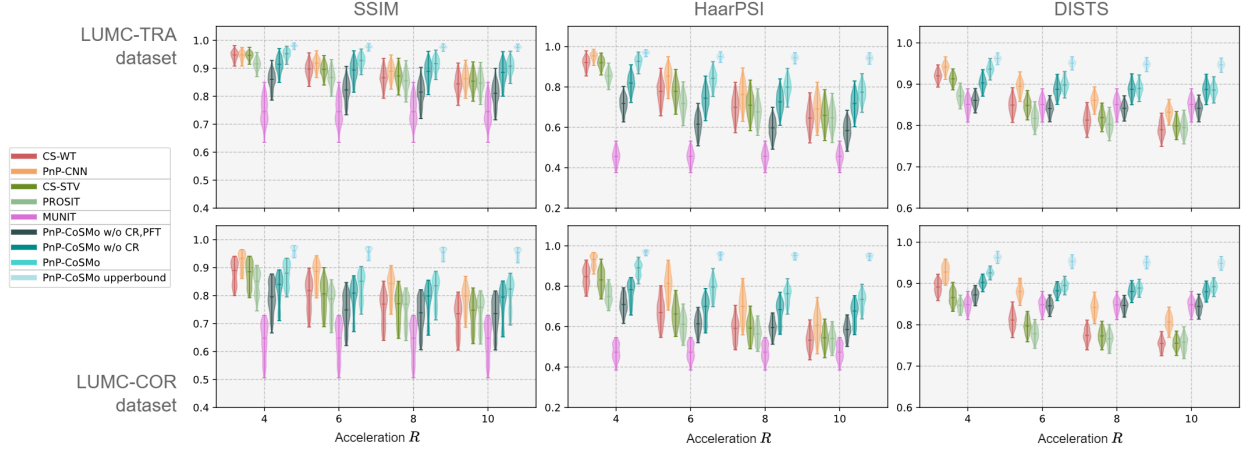


Figure 10: Evaluation plots over *recon-test* subset of LUMC-TRA and LUMC-COR datasets consisting of 1366 and 200 slices, respectively.

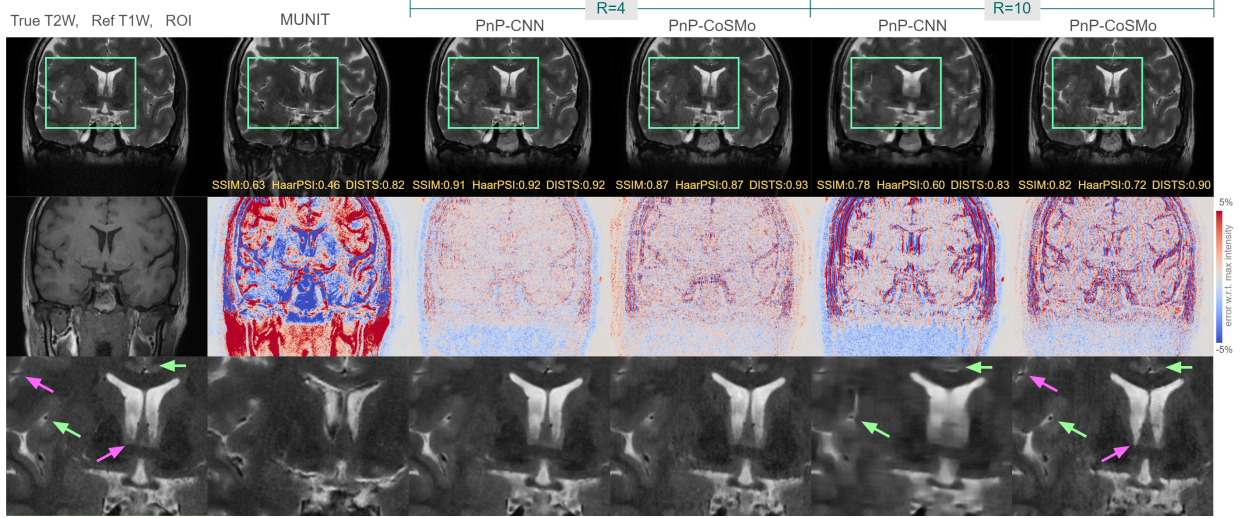


Figure 11: Sample slice from the LUMC-COR *recon-test* set comparing PnP-CoSMo with PnP-CNN and MUNIT image translation.

5.3. Benchmark and ablation on the LUMC multi-coil data

The LUMC datasets represent a more challenging problem with real-world data constraints. Additionally, in the light of the content capacity analysis (Section 5.1.2), we empirically found that the content capacity $J_M=1/4$ was optimal for the LUMC datasets, compared to NYU DICOM data where $J_M=1$ was the optimal content capacity. This reflects the lower effective content in LUMC image data and hence a greater difficulty of the guided reconstruction problem.

Fig. 10 plots the benchmark metrics for the LUMC test sets, which can be summarized in the following three trends. First, pure image translation with MUNIT was worse compared to single-contrast reconstruction, especially at lower acceleration factors (comparing with PnP-CNN, $p<0.05$ for all metrics and both datasets). Combining it with L2-regularized reconstruction in PROSIT improved SSIM and HaarPSI ($p<0.05$ for both datasets and accelerations), but not necessarily DISTS, suggesting that the available complementary information was not fully utilized. PnP-CoSMo was consistently better than both MUNIT image translation and PROSIT ($p<0.05$ throughout for both cases). It also outperformed the conventional

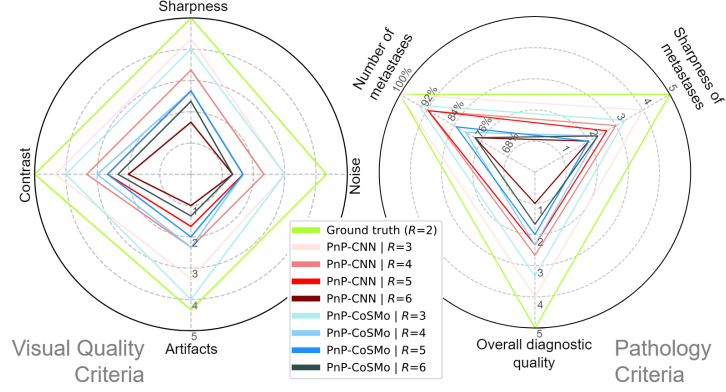


Figure 12: Scores from the radiological evaluation averaged over the three subjects.

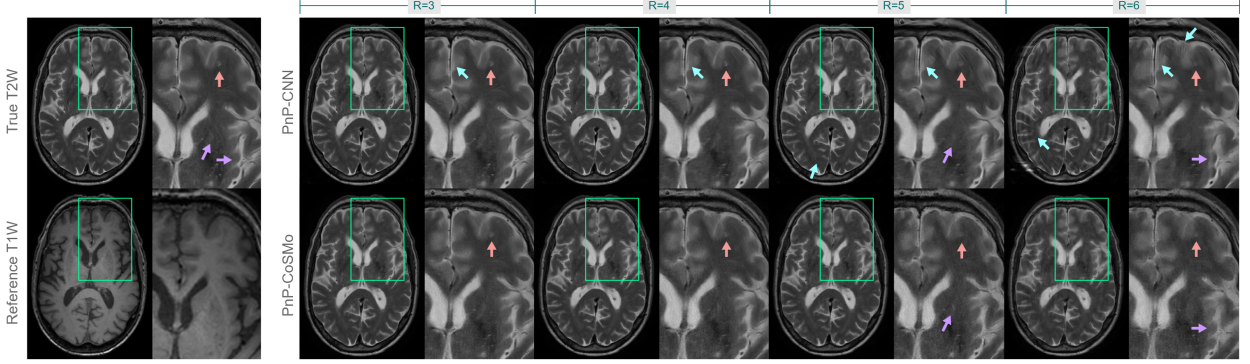


Figure 13: Example slice from the LUMC-TRA subset used in the radiological evaluation. Several relevant features are marked including a brain metastasis-related hyperintense feature (salmon-pink arrows), reconstruction artifacts (cyan arrows), and blurring (purple arrows).

guided CS-STV ($p < 0.05$ throughout, except SSIM at $R=4$ in LUMC-COR). Hence, using both measured k-space and reference scan via PnP-CoSMo was more beneficial than (a) using either one of them and (b) combining both using hand-crafted priors, suggesting that our approach maximally exploits the complementary information. Second, both PnP-CNN and PnP-CoSMo performed similarly at lower acceleration, except in terms of SSIM and HaarPSI at $R=4$ and $R=6$ on LUMC-COR where PnP-CNN was slightly better. At higher acceleration, PnP-CoSMo outperformed PnP-CNN ($p < 0.05$ for all metrics and both datasets except SSIM at $R=8$ in LUMC-COR). Compared to PnP-CNN, PnP-CoSMo allowed up to 32.6% more acceleration for a given SSIM.² Third, introducing PFT and CR into the ablated PnP-CoSMo improved the reconstructions ($p < 0.05$ throughout in both cases except in DISTS for the latter at $R=10$ in LUMC-TRA). The contribution of PFT was almost constant across R , whereas that of CR decreased as R increased, which was expected since CR depends on the measured k-space data to refine the content.

Fig. 11 shows an LUMC-COR example representative of the first two trends. MUNIT image translation produced severe anatomical defects and predicted false structure in the lower region of the image where the ground truth, in fact, contains low signal. At $R=4$, PnP-CoSMo was visually similar to PnP-CNN, with the main difference being a blur effect in PnP-CNN and mild texture artifacts in PnP-CoSMo. At $R=10$, PnP-CNN reconstruction was non-viable, containing severe blur and artifacts (green arrows). On the other hand, PnP-CoSMo did not degrade much from the $R=4$ case and most fine structures were sharply resolved

²Based on linear interpolation of LUMC-TRA SSIM, PnP-CoSMo and PnP-CNN allowed $R=10$ and $R=6.7$, which is the maximum difference in R , at median SSIM=0.906. Hence, a difference of 32.6%.

(green arrows). However, an interesting failure mode of PnP-CoSMo at high acceleration was the subtle localized distortions in the anatomy (magenta arrows).

5.4. Radiological evaluation

Figure 12 plots the radiological evaluation result. At $R=3$, both algorithms produced diagnostic-quality reconstructions, a difference of 33.3% of k-space samples over the clinical reconstructions of $R=2$. PnP-CNN was slightly better than PnP-CoSMo at $R \in \{3, 4\}$ in terms of sharpness, contrast, and the pathology criteria. At $R=5$, PnP-CoSMo matched or exceeded PnP-CNN in terms of visual quality, although being worse in terms of pathology criteria. At $R=6$, PnP-CNN sharply dropped to the "non-diagnostic" level, whereas PnP-CoSMo was better, especially in terms of sharpness and contrast as well as in overall diagnostic quality. This trend is illustrated with a representative example in Figure 13. While the $R=3$ reconstructions of PnP-CNN and PnP-CoSMo are of a similarly high quality, reconstruction artifacts (cyan arrows) become more pronounced in PnP-CNN reconstructions with increasing acceleration. At $R=6$, compared to PnP-CoSMo, the PnP-CNN reconstruction has severe artifacts, blurrier and more distorted features (purple arrows), and a poorly visible hyperintense area of a brain metastasis (salmon-pink arrows).

6. Discussion

In this work, we modeled two-contrast MR image data in terms of two latent generative factors – *content* representing the contrast-independent structure and *style* representing the contrast-specific variations. Our data-driven definitions of content and style, though seemingly related to the MR physics-based representations of quantitative maps and acquisition-related factors, are rather nebulous compared to precisely defined physical concepts. For instance, MR quantitative maps are theoretically objective representations of tissues in terms of physical variables such as relaxation times and are ideally independent of the contrast-generating sequence parameters. On the other hand, our content and style representations are only defined statistically in terms of the given two contrasts and are, thus, neither as objective nor as independent in the ideal physical sense. That being said, we would argue that there is potential value in augmenting the data-driven content/style model with MR physical models, e.g. by constraining the learned content to represent physically meaningful anatomical properties, introducing elements of a physical model (e.g. Bloch equations) into the decoder network, etc., to enhance interpretability and reconstruction quality.

Optimal content capacity was defined as a quantity representing the amount of shared local information contained in a two-contrast dataset. In terms of this quantity, we analyzed the effect of reference image resolution on reconstruction quality, obtaining a lowerbound for PnP-CoSMo to be effective (Section 5.1.2). This quantity would depend on more fundamental factors such as MR sequence types, which we did not investigate here. While we limited our experiments to T1W and T2W sequences, PnP-CoSMo is, in principle, applicable to any pair of contrasts, with the image quality limited mainly by the amount of structural information shared between them. Future work could help empirically determine which sequence pairs are more amenable to guided reconstruction than others. A consequence of our MUNIT-based model design was the model’s lack of dependence on the uni-directionality of the guided reconstruction problem, which allowed greater generalizability by design (Section 5.2). It is, in principle, also possible to model the content and style for more than two contrasts. This would enable not only the generalizability of our approach to any combinatorial set of guided reconstruction tasks, but also better estimation of the target contrast’s content by utilizing multiple reference contrasts in the reconstruction. Given number of contrasts N , content could be defined as the local structure underlying all these contrasts, while style would encode intra-contrast variations of each individual contrast. This model would then require an (unpaired) image-domain training dataset of the N contrasts. An open question is how to effectively scale the model and training complexity to N contrasts. The PnP-CoSMo algorithm can subsequently be extended to utilize multiple reference contrasts to guide a given target contrast. The specific question to investigate then would be – given P reference contrasts (where $1 < P < N$), how to aggregate their contents such that the prior structural information about the target image is maximized?

Content discrepancy was characterized as a quantity representing the gap between the true content of the target image and our estimation of this content, which is another limiting factor in PnP-CoSMo

reconstruction. In our MUNIT-based network design, the decoders model the (forward) generative process that maps the latent variables (i.e. content and style) to the observable variable (i.e. images). Ideally, the encoders must be a perfect inverse of this forward process. However, estimating the multi-channel contrast-independent content from a single image (using the content encoders) is a challenging (and perhaps ill-conditioned) inverse problem. Hence, some errors are to be expected in the content estimated from the reference image. Moreover, the reference image may contain unfavorable differences from the target image, such as misalignment or artifacts, which introduce more errors. Therefore, content discrepancy is expected to be a non-zero quantity. We proposed two complementary ways to minimize its effect on the reconstruction. While paired fine-tuning improves the model using a small amount of paired image-domain training data, content refinement (CR) aims to correct the remaining discrepancy during reconstruction using the measured k-space. A drawback of the CR module, however, is slower convergence (Section 5.1.3). For example, the run-time for PnP-CoSMo on the GPU was around 17 seconds for a slice of matrix size 349×284 , as compared to 6 seconds for CS-WT, 1.4 seconds for PnP-CNN, and less than 0.1 second for MC-VarNet. This latency issue could be mitigated by approximating the iterative process with an unrolled network design, although potentially at a cost of the generalizability offered by the plug-and-play design. The resulting trade-off between model latency and generalizability would be interesting to explore in the future.

In terms of training data requirements, PnP-CoSMo can make use of the larger amounts of the image data available and can be applied to situations where end-to-end methods are infeasible since it does not rely on k-space training data. In situations where end-to-end methods are indeed feasible, PnP-CoSMo is comparable to state-of-the-art methods in terms of metrics and superior in terms of visual quality, especially at higher accelerations (Section 5.2). Moreover, unpaired image-domain pre-training of the content/style model boosts the practical applicability of PnP-CoSMo, e.g. in the case of LUMC-TRA where the T1W/T2W data imbalance was considerable. As indicated in our NYU DICOM benchmark, PnP-CoSMo performs similarly or better than state-of-the-art end-to-end methods. In our LUMC multi-coil benchmark, we limited our baselines to those algorithms that were feasible given the data constraint. As future work, a more comprehensive study should be conducted with a broader range of methods and evaluation criteria, e.g. comparing generalizability across accelerations and sampling patterns with multi-contrast unrolled networks, given a fixed budget of paired training data. Contrary to the training stage, we strictly assumed the spatial alignment of the reference and target images in the reconstruction stage. The CR module, which can implicitly correct minor registration errors, would likely break down at the typically observed levels of patient motion. A potential solution is to incorporate an online registration step to explicitly and efficiently correct for arbitrary inter-scan motion, thereby further improving practical applicability.

In terms of reconstruction quality, we observed in Section 5.3 that the true added value of PnP-CoSMo was at the high acceleration factors ($R=8$ and $R=10$) where the k-space data is scarce and the reference information becomes more valuable. However, the risk of model hallucinations increases at these accelerations, raising concerns about the accuracy of the anatomy represented in the image. We hypothesize that as a consequence of content/style decomposition, it may be possible to leverage the contrast-independence property of the content to – (a) automatically detect local hallucinations in the reconstruction and (b) define a corrective process in combination with an adaptive sampling strategy to minimize it. This is yet another topic for future work. At lower accelerations, on the other hand, we observed that PnP-CoSMo often produced slightly lower metrics compared to PnP-CNN, e.g. in LUMC-COR. This was also observed in the radiological evaluation on LUMC-TRA samples. This is counter-intuitive at first glance since PnP-CoSMo has access to additional side information and should, in principle, perform at least as well as PnP-CNN. However, this can be explained by the fact that at lower accelerations, the content/style model becomes the main limiting factor for reconstruction quality. This is because unlike the CNN denoiser (Eq. (4)) of PnP-CNN, the content consistency operator (Eq. (15)) of PnP-CoSMo radically alters the image and hence, this operation is sensitive to the model’s overall performance. The model performance is in turn influenced by the training dataset and the network architecture. First, regarding data, the T1W scans in LUMC datasets had an in-plane resolution 1.3-2.5 times lower than that of the T2W scans, limiting the quality of the model (as indicated by its low optimal content capacity) and the overall value of guidance. In the long run, this may be solved by using 3D reference and target sequences of matched-resolution to optimize

guidance. Second, regarding model design, correcting for content discrepancy using the CR module relies on computing gradients through the decoder G_2 (Eq. (17)). If G_2 is highly non-linear and the reference content is not sufficiently close to the optimum, CR may converge to a sub-optimal point leading to texture artifacts in the reconstruction, as seen in Fig. 11 at $R=4$. In our proof-of-concept, we used the same general model architecture proposed in Huang et al. (2018). Better designs that are more conducive to CR may exist. Hence, future efforts must considerably focus on improving the content/style model using specialized architecture and regularization.

7. Conclusion

In this work, we introduced PnP-CoSMo, a modular approach to multi-contrast reconstruction which combines content/style modeling with iterative reconstruction, offering the reconstruction quality of state-of-the-art end-to-end methods with improved generalizability despite lenient training data requirements. At its core is the content consistency operation, which provides regularization at the semantic level of the image content. We defined two quantities that determine the efficacy of this operation, namely optimal content capacity and content discrepancy, and provided several ways of maximizing this efficacy. On real-world clinical data, PnP-CoSMo provided up to 32.6% more acceleration over PnP-CNN for given SSIM, enabling sharper reconstructions at high accelerations. In the radiological task of visual quality assessment and brain metastasis diagnosis at realistic accelerations, PnP-CoSMo produced diagnostic-quality images at $R=3$, enabling 33.3% more acceleration over clinical reconstructions. To progress towards practical implementation of our proof-of-concept, future work will focus mainly on improving and extending the content/style model, reducing reconstruction latency, tackling the problem of model hallucinations, and incorporating online registration into the reconstruction.

CRedit authorship contribution statement

Chinmay Rao: Conceptualization, Methodology, Data curation, Software, Investigation, Validation, Formal analysis, Visualization, Writing – original draft. **Matthias van Osch:** Funding acquisition, Supervision, Conceptualization, Validation, Writing – review & editing. **Nicola Pezzotti:** Funding acquisition, Supervision, Conceptualization, Methodology, Validation. **Jeroen de Bresser:** Investigation, Validation. **Laurens Beljaards:** Data curation, Software. **Jakob Meineke:** Resources, Software. **Elwin de Weerdt:** Conceptualization, Resources. **Huangling Lu:** Investigation. **Mariya Doneva:** Supervision, Conceptualization, Methodology, Validation, Writing – review & editing. **Marius Staring:** Funding acquisition, Project administration, Supervision, Conceptualization, Methodology, Validation, Writing – review & editing.

Declaration of competing interest

The authors declare the following financial interests or personal relationships which may be considered as potential competing interests: Chinmay Rao and Laurens Beljaards declare the grant and research support they receive received from Philips. Nicola Pezzotti, Jakob Meineke, Elwin de Weerdt, and Mariya Doneva declare their employment at Philips. Given his role as Associate Editor, Marius Staring had no involvement in the peer review of this article and had no access to information regarding its peer review. Full responsibility for the editorial process for this article was delegated to another journal editor. If there are other authors, they declare that they have no known competing financial interests or personal relationships that could have appeared to influence the work reported in this paper.

Acknowledgments

This work is part of the project ROBUST: Trustworthy AI-based Systems for Sustainable Growth with project number KICH3.LTP.20.006, which is (partly) financed by the Dutch Research Council (NWO), Philips Research, and the Dutch Ministry of Economic Affairs and Climate Policy (EZK) under the program LTP KIC 2020-2023.

Data availability

The authors do not have permission to share data.

References

- Aggarwal, H.K., Mani, M.P., Jacob, M., 2018. MoDL: Model-based Deep Learning Architecture for Inverse Problems. *IEEE Transactions on Medical Imaging* 38, 394–405.
- Ahmad, R., Bouman, C.A., Buzzard, G.T., Chan, S., Liu, S., Reehorst, E.T., Schniter, P., 2020. Plug-and-play Methods for Magnetic Resonance Imaging using Denoisers for Image Recovery. *IEEE Signal Processing Magazine* 37, 105–116.
- Atli, O.F., Kabas, B., Arslan, F., Demirtas, A.C., Yurt, M., Dalmaz, O., Çukur, T., 2024. I2i-mamba: Multi-modal medical image synthesis via selective state space modeling. *arXiv preprint arXiv:2405.14022*.
- Bilgic, B., Goyal, V.K., Adalsteinsson, E., 2011. Multi-contrast Reconstruction with Bayesian Compressed Sensing. *Magnetic Resonance in Medicine* 66, 1601–1615.
- Boyd, S., Parikh, N., Chu, E., Peleato, B., Eckstein, J., et al., 2011. Distributed optimization and statistical learning via the alternating direction method of multipliers. *Foundations and Trends® in Machine learning* 3, 1–122.
- Chambolle, A., De Vore, R.A., Lee, N.Y., Lucier, B.J., 1998. Nonlinear Wavelet Image Processing: Variational Problems, Compression, and Noise Removal through Wavelet Shrinkage. *IEEE Transactions on Image Processing* 7, 319–335.
- Collins, D.L., Zijdenbos, A.P., Kollokian, V., Sled, J.G., Kabani, N.J., Holmes, C.J., Evans, A.C., 1998. Design and Construction of a Realistic Digital Brain Phantom. *IEEE Transactions on Medical Imaging* 17, 463–468.
- Dar, S.U., Yurt, M., Karacan, L., Erdem, A., Erdem, E., Çukur, T., 2019. Image Synthesis in Multi-Contrast MRI With Conditional Generative Adversarial Networks. *IEEE Transactions on Medical Imaging* 38, 2375–2388. doi:10.1109/TMI.2019.2901750.
- Dar, S.U., Yurt, M., Shahdloo, M., Ildiz, M.E., Tınaz, B., Çukur, T., 2020. Prior-Guided Image Reconstruction for Accelerated Multi-Contrast MRI via Generative Adversarial Networks. *IEEE Journal of Selected Topics in Signal Processing* 14, 1072–1087. doi:10.1109/JSTSP.2020.3001737.
- Denck, J., Guehring, J., Maier, A., Rothgang, E., 2021. MR-contrast-aware Image-to-Image Translations with Generative Adversarial Networks. *International Journal of Computer Assisted Radiology and Surgery* 16. doi:10.1007/s11548-021-02433-x.
- Ehrhardt, M.J., Betcke, M.M., 2016. Multicontrast MRI Reconstruction with Structure-Guided Total Variation. *SIAM Journal on Imaging Sciences* 9, 1084–1106. doi:10.1137/15M1047325.
- Feng, C.M., Yan, Y., Chen, G., Xu, Y., Hu, Y., Shao, L., Fu, H., 2022. Multimodal transformer for accelerated mr imaging. *IEEE Transactions on Medical Imaging* 42, 2804–2816.
- Griswold, M.A., Jakob, P.M., Heidemann, R.M., Nittka, M., Jellus, V., Wang, J., Kiefer, B., Haase, A., 2002. Generalized Autocalibrating Partially Parallel Acquisitions (GRAPPA). *Magnetic Resonance in Medicine* 47, 1202–1210.
- Huang, J., Chen, C., Axel, L., 2014. Fast Multi-contrast MRI Reconstruction. *Magnetic Resonance Imaging* 32, 1344–1352.

- Huang, X., Liu, M.Y., Belongie, S., Kautz, J., 2018. Multimodal Unsupervised Image-to-Image Translation, in: *Proceedings of the European Conference on Computer Vision (ECCV)*, pp. 172–189.
- Isola, P., Zhu, J.Y., Zhou, T., Efros, A.A., 2017. Image-to-image Translation with Conditional Adversarial Networks, in: *Proceedings of the IEEE Conference on Computer Vision and Pattern Recognition*, pp. 1125–1134.
- Kamilov, U.S., Bouman, C.A., Buzzard, G.T., Wohlberg, B., 2023. Plug-and-play Methods for Integrating Physical and Learned Models in Computational Imaging: Theory, Algorithms, and Applications. *IEEE Signal Processing Magazine* 40, 85–97. Publisher: IEEE.
- Kastrýulin, S., Zakirov, J., Pezzotti, N., Dylov, D.V., 2023. Image Quality Assessment for Magnetic Resonance Imaging. *IEEE Access* 11, 14154–14168. Publisher: IEEE.
- Klein, S., Staring, M., Murphy, K., Viergever, M.A., Pluim, J.P., 2009. Elastix: A Toolbox for Intensity-based Medical Image Registration. *IEEE Transactions on Medical Imaging* 29, 196–205.
- Knoll, F., Zbontar, J., Sriram, A., Muckley, M.J., Bruno, M., Defazio, A., Parente, M., Geras, K.J., Katsnelson, J., Chandarana, H., et al., 2020. fastMRI: A Publicly Available Raw k-space and DICOM Dataset of Knee Images for Accelerated MR Image Reconstruction using Machine Learning. *Radiology: Artificial Intelligence* 2, e190007.
- Kopanoglu, E., Güngör, A., Kilic, T., Saritas, E.U., Oguz, K.K., Çukur, T., Güven, H.E., 2020. Simultaneous Use of Individual and Joint Regularization Terms in Compressive Sensing: Joint Reconstruction of Multi-channel Multi-contrast MRI Acquisitions. *NMR in Biomedicine* 33, e4247.
- Kotovenko, D., Sanakoyeu, A., Lang, S., Ommer, B., 2019. Content and style disentanglement for artistic style transfer, in: *Proceedings of the IEEE/CVF International Conference on Computer Vision (ICCV)*.
- Kwon, G., Ye, J.C., 2021. Diagonal attention and style-based gan for content-style disentanglement in image generation and translation, in: *Proceedings of the IEEE/CVF International Conference on Computer Vision (ICCV)*, pp. 13980–13989.
- Lei, P., Fang, F., Zhang, G., Zeng, T., 2023. Decomposition-based variational network for multi-contrast mri super-resolution and reconstruction, in: *Proceedings of the IEEE/CVF International Conference on Computer Vision*, pp. 21296–21306.
- Levac, B., Jalal, A., Ramchandran, K., Tamir, J.I., 2023. Mri reconstruction with side information using diffusion models, in: *2023 57th Asilomar Conference on Signals, Systems, and Computers*, IEEE. pp. 1436–1442.
- Liu, M.Y., Breuel, T., Kautz, J., 2017. Unsupervised Image-to-image Translation Networks. *Advances in Neural Information Processing Systems* 30.
- Liu, X., Wang, J., Lin, S., Crozier, S., Liu, F., 2021a. Optimizing Multicontrast MRI Reconstruction with Shareable Feature Aggregation and Selection. *NMR in Biomedicine* 34, e4540.
- Liu, X., Wang, J., Sun, H., Chandra, S.S., Crozier, S., Liu, F., 2021b. On the Regularization of Feature Fusion and Mapping for Fast MR Multi-contrast Imaging via Iterative Networks. *Magnetic Resonance Imaging* 77, 159–168.
- Lustig, M., Donoho, D., Pauly, J.M., 2007. Sparse MRI: The Application of Compressed Sensing for Rapid MR Imaging. *Magnetic Resonance in Medicine* 58, 1182–1195.
- Mason, A., Rioux, J., Clarke, S.E., Costa, A., Schmidt, M., Keough, V., Huynh, T., Beyea, S., 2019. Comparison of Objective Image Quality Metrics to Expert Radiologists’ Scoring of Diagnostic Quality of MR Images. *IEEE Transactions on Medical Imaging* 39, 1064–1072.

- Mattern, H., Sciarra, A., Dünnwald^o, M., Chatterjee, S., Müller, U., Oetze-Jafra^o, S., Speck, O., 2020. Contrast Prediction-based Regularization for Iterative Reconstructions (PROSIT), in: International Society for Magnetic Resonance in Medicine (ISMRM).
- Miyato, T., Kataoka, T., Koyama, M., Yoshida, Y., 2018. Spectral normalization for generative adversarial networks. arXiv preprint arXiv:1802.05957 .
- Oh, G., Sim, B., Chung, H., Sunwoo, L., Ye, J.C., 2020. Unpaired Deep Learning for Accelerated MRI using Optimal Transport Driven CycleGAN. *IEEE Transactions on Computational Imaging* 6, 1285–1296.
- Pezzotti, N., Yousefi, S., Elmahdy, M.S., Van Gemert, J.H.F., Schuelke, C., Doneva, M., Nielsen, T., Kastrulin, S., Lelieveldt, B.P.F., Van Osch, M.J.P., De Weerd, E., Staring, M., 2020. An Adaptive Intelligence Algorithm for Undersampled Knee MRI Reconstruction. *IEEE Access* 8, 204825–204838. doi:10.1109/ACCESS.2020.3034287.
- Pingfan, S., Weizman, L., MOTA, J., et al., 2018. Coupled dictionary learning for multi-contrast mri reconstruction, in: The 25th IEEE International Conference on Image Processing, Athens, Greece, pp. 2880–2884.
- Pooja, K., Ramzi, Z., Chaithya, G., Ciuciu, P., 2022. Mc-pdnet: Deep Unrolled Neural Network for Multi-contrast MR Image Reconstruction from Undersampled k-space Data, in: IEEE International Symposium on Biomedical Imaging (ISBI), IEEE. pp. 1–5.
- Pruessmann, K.P., Weiger, M., Börnert, P., Boesiger, P., 2001. Advances in sensitivity encoding with arbitrary k-space trajectories. *Magnetic Resonance in Medicine* 46, 638–651.
- Rao, C., Beljaards, L., van Osch, M., Doneva, M., Meineke, J., Schuelke, C., Pezzotti, N., de Weerd, E., Staring, M., 2024. Guided Multicontrast Reconstruction based on the Decomposition of Content and Style, in: International Society for Magnetic Resonance in Medicine (ISMRM).
- Richardson, E., Weiss, Y., 2021. The Surprising Effectiveness of Linear Unsupervised Image-to-Image Translation, in: 2020 25th International Conference on Pattern Recognition (ICPR), pp. 7855–7861. doi:10.1109/ICPR48806.2021.9413199.
- Schlemper, J., Caballero, J., Hajnal, J.V., Price, A.N., Rueckert, D., 2017. A Deep Cascade of Convolutional Neural Networks for Dynamic MR Image Reconstruction. *IEEE Transactions on Medical Imaging* 37, 491–503.
- Seow, P., Kheok, S.W., Png, M.A., Chai, P.H., Yan, T.S.T., Tan, E.J., Liauw, L., Law, Y.M., Anand, C.V., Lee, W., et al., 2024. Evaluation of Compressed SENSE on Image Quality and Reduction of MRI Acquisition Time: A Clinical Validation Study. *Academic Radiology* 31, 956–965.
- Wang, Q., Wen, Z., Shi, J., Wang, Q., Shen, D., Ying, S., 2024. Spatial and modal optimal transport for fast cross-modal mri reconstruction. *IEEE Transactions on Medical Imaging* .
- Weizman, L., Eldar, Y.C., Ben Bashat, D., 2016. Reference-based MRI. *Medical Physics* 43, 5357–5369.
- Wu, Y., Nakashima, Y., Garcia, N., 2023. Not only generative art: Stable diffusion for content-style disentanglement in art analysis, in: Proceedings of the 2023 ACM International conference on multimedia retrieval, pp. 199–208.
- Xuan, K., Xiang, L., Huang, X., Zhang, L., Liao, S., Shen, D., Wang, Q., 2022. Multimodal MRI Reconstruction Assisted with Spatial Alignment Network. *IEEE Transactions on Medical Imaging* 41, 2499–2509.
- Yang, Y., Wang, N., Yang, H., Sun, J., Xu, Z., 2020. Model-driven Deep Attention Network for Ultra-fast Compressive Sensing mri Guided by Cross-contrast MR Image, in: Medical Image Computing and Computer Assisted Intervention (MICCAI), Springer. pp. 188–198.

- Yurt, M., Dar, S.U., Erdem, A., Erdem, E., Oguz, K.K., Çukur, T., 2021. mustGAN: Multi-stream Generative Adversarial Networks for MR Image Synthesis. *Medical Image Analysis* 70, 101944. doi:10.1016/j.media.2020.101944.
- Zbontar, J., Knoll, F., Sriram, A., Murrell, T., Huang, Z., Muckley, M., Defazio, A., Stern, R., Johnson, P., Bruno, M., et al., 1811. fastMRI: An Open Dataset and Benchmarks for Accelerated MRI. *arXiv preprint arXiv:1811.08839* .
- Zhou, B., Zhou, S.K., 2020. DuDoRNet: Learning a Dual-domain Recurrent Network for Fast MRI Reconstruction with Deep T1 Prior, in: *Proceedings of the IEEE/CVF Conference on Computer Vision and Pattern Recognition*, pp. 4273–4282.
- Zhu, J.Y., Park, T., Isola, P., Efros, A.A., 2017. Unpaired Image-to-image Translation using Cycle-consistent Adversarial Networks, in: *Proceedings of the IEEE International Conference on Computer Vision*, pp. 2223–2232.